Brazilian Journal of Physics (2022) 52:87
https://doi.org/10.1007/s13538-022-01085-9

GENERAL AND APPLIED PHYSICS

Electron Acceleration by Quasilinear Processes in the Presence of a Ring-beam Electron Population

Luiz F. Ziebell[1] · Peter H. Yoon[2]

Received: 25 January 2022 / Accepted: 1 March 2022

Abstract
A set of self-consistent equations of weak turbulence theory that describe the time evolution of the electron velocity distribution and of the spectra of Langmuir and ion sound waves is solved numerically, considering the presence of a core electron population and a ring-beam electron distribution. The results obtained show that the finite pitch angle of the beam relative to the direction of the ambient magnetic field leads to a spectrum of Langmuir waves which is more complex than the spectrum obtained in the case of beams with zero pitch angle, to an enlarged *plateau* in the beam region of the electron velocity distribution and to the generation of a prominent high-velocity population in the electron velocity distribution.

Keywords Beam-plasma instability · Electron acceleration · Energetic electron tails · Weak turbulence · Ring-beam distributions

1 Introduction

Plasmas in space environments frequently have electron populations with drifting motion relative to the background population, a configuration which can provide the energy for plasma instabilities. In the solar wind, these drifting populations sometimes can be in the form of electron beams propagating in the forward or backward direction along the magnetic field lines, but sometimes they may feature significant perpendicular velocity in addition to velocity along the magnetic field lines. A drifting electron velocity distribution with such configuration constitutes the so-called *ring-beam* distribution [1–4]. For instance, it is well known that an effective ring-beam electron velocity distribution in the so-called de-Hoffman-Teller frame forms as a result of the upstream solar wind electrons interacting at the quasi-perpendicular bow shock [5] or at the front of the coronal mass ejection (CME) shock [6]. Such ring-beam electron distribution functions have been investigated in the context of radio bursts (type II solar radio or multiple-harmonic plasma emission at the Earths bow shock) [6–8].

In a recently published paper, one of us also investigated the beam-plasma instability and the consequent emission of transverse waves, using weak turbulence theory and considering a small population of electrons with a finite pitch distribution drifting along the direction of the magnetic field, through the ambient plasma [9]. The results obtained in that investigation have shown that the existence of a finite pitch angle leads to structures in the spectra of electrostatic waves which are more complex than those obtained in the case of distributions simply drifting along the magnetic field, without pitch angle. It has also been observed in the results the emission of a spectrum of transverse waves similar to that obtained considering zero pitch angle in the beam drift, but with enhanced emission at harmonics of the fundamental frequency. This work is thus relevant to the above-stated radio burst problem at the collisionless shock although such a direct connection has not been stated in ref. [9]. Regarding the electron velocity distribution, the results obtained have shown the formation of an enlarged *plateau* in the region of the beam, in velocity space. It has also been observed some growth of the population of electrons in the region of high parallel velocity [9].

The results obtained in Ziebell [9] have motivated us to proceed with further analysis, with focus on the possibility

✉ Luiz F. Ziebell
luiz.ziebell@ufrgs.br

Peter H. Yoon
yoonp@umd.edu

[1] Instituto de Física, Universidade Federal do Rio Grande do Sul, Porto Alegre 91501-970, RS, Brazil

[2] Institute for Physical Science and Technology, University of Maryland, College Park, MD 20742-243, USA

Published online: 31 March 2022

of electron acceleration in the case of significant pitch angle in the population of drifting electrons. In the present paper, we present results originated from this investigation. As in Ziebell (2021), the analysis is made using equations of weak turbulence theory, but here we take into account only the presence of Langmuir and ion sound waves and neglect effects associated with transverse waves. The sequence of the paper is organized as follows: Sect. 2 briefly presents the model which is utilized in the investigation, including the mathematical form of the electron velocity distribution function and some general features of the theoretical formulation. Section 3 briefly discusses the procedures for numerical solution of the system of coupled evolution equations, and present some results that show the spectrum of Langmuir waves and the electron distribution function, for different values of time. At the end, Sect. 4 presents a summary of the results obtained.

2 Modeling and Theoretical Framework

As an initial condition, the electron velocity distribution is assumed to be a summation of a Maxwellian core and a ring-beam distribution. Assuming that the electron number density is n_e and the beam number density is n_{ef}, this velocity distribution can be written as follows,

$$f_e(\mathbf{v}) = \left(1 - \frac{n_{ef}}{n_e}\right) f_{e,M}(\mathbf{v}) + \frac{n_{ef}}{n_e} f_{e,f}(\mathbf{v}), \tag{1}$$

where

$$f_{e,M}(\mathbf{v}) = \frac{1}{\pi^{3/2} v_e^3} \exp\left(-\frac{v_\perp^2 + (v_\parallel - v_0)^2}{v_e^2}\right), \tag{2}$$

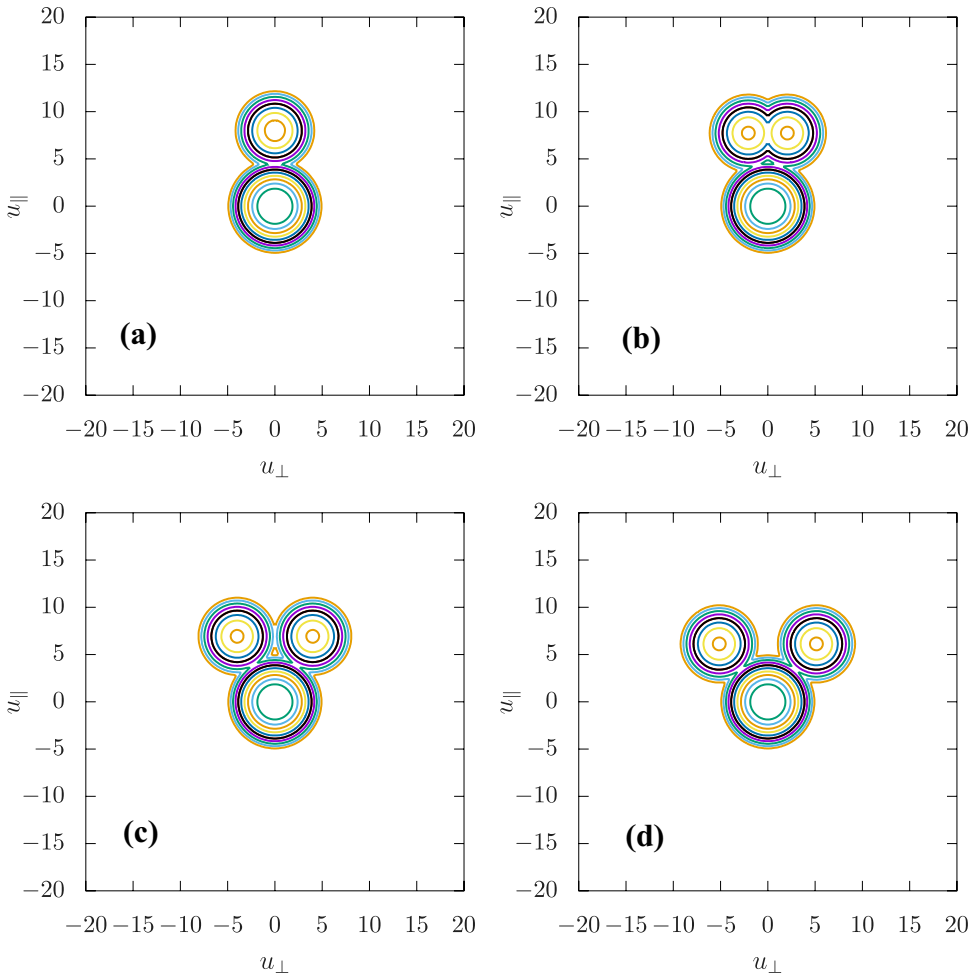

Fig. 1 Surface plots of the normalized electron distribution function in logarithmic scale, in bi-dimensional normalized velocity space, at $\tau = 100$. **a** $\theta_f = 0°$; **b** $\theta_f = 15°$; **c** $\theta_f = 30°$; **d** $\theta_f = 40°$. Other parameters are $\left(n_e \lambda_{De}^3\right)^{-1} = 5.0 \times 10^{-3}$, $n_{fe}/n_e = 1.0 \times 10^{-3}, U_f = 8.0$, $T_f/T_e = 1.0, T_e/T_i = 2.0$. The surface plots show 11 levels, between 1×10^{-11} and 1×10^{-2} (the more internal level, at the core distribution). Results obtained taking into account spontaneous and induced emission in the equation for evolution of Langmuir waves

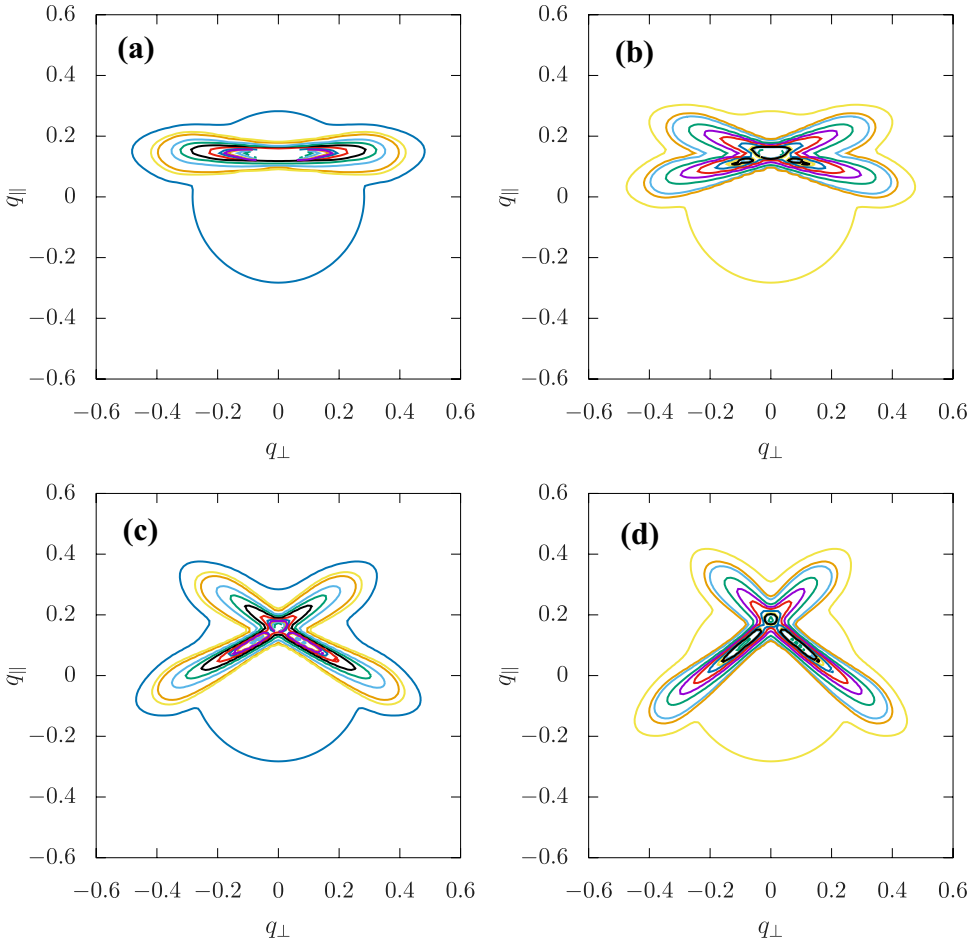

Fig. 2 Surface plots of the normalized spectrum of Langmuir waves in logarithmic scale, vs. $q_\parallel = k_\parallel v_e/\omega_{pe}$ and $q_\perp = k_\perp v_e/\omega_{pe}$, at $\tau = 100$. **a** $\theta_f = 0°$; **b** $\theta_f = 15°$; **c** $\theta_f = 30°$; **d** $\theta_f = 40°$. The surface plots show 13 levels, between 5×10^{-6} (the more external level) and 5×10^{-3}. Other parameters and conditions are as in Fig. 1

$$f_{e,f}(\mathbf{v}) = \frac{1}{\pi^{3/2} v_e^3} \exp\left(- \frac{(v_\perp - v_{f\perp})^2 + (v_\parallel - v_{f\parallel})^2}{v_e^2} \right). \tag{3}$$

The beam speed is v_f and the beam pitch angle is θ_f, so that $v_{f\perp} = v_f \sin\theta_f$, $v_{f\parallel} = v_f \cos\theta_f$. The Maxwellian core distribution features a drift velocity $v_0 = -n_{ef} v_f \cos\theta_f/(n_e - n_{ef})$, such that the electron population remains current-free. The distributions (2) and (3) also feature the thermal velocity of the electrons, given by $v_e = \sqrt{2T_e/m_e}$, where T_e is the electron temperature written in energy units and m_e is the electron mass. For the ion velocity distribution, f_i, we assume a Maxwellian distribution, which does not change along time evolution.

The set of equations which is utilized in the present analysis can be found in the literature, as in ref. [10], for instance. Nevertheless, they are reproduced here for the sake of completeness.

For the electron distribution function, we consider a time evolution equation which features a quasilinear diffusion term and also a term associated with spontaneous fluctuations [10],

$$\frac{\partial f_e(\mathbf{v})}{\partial t} = \frac{\pi e^2}{m_e^2} \sum_{\sigma=\pm 1} \sum_{\alpha=L,S} \int d\mathbf{k}\, \frac{\mathbf{k}}{k} \cdot \frac{\partial}{\partial \mathbf{v}}\, \delta(\sigma\omega_{\mathbf{k}}^\alpha - \mathbf{k}\cdot\mathbf{v}) \times \left(\frac{m_e}{4\pi^2} \frac{\sigma\omega_{\mathbf{k}}^\alpha}{k} f_e(\mathbf{v}) + I_{\mathbf{k}}^{\sigma\alpha} \frac{\mathbf{k}}{k} \cdot \frac{\partial f_e(\mathbf{v})}{\partial \mathbf{v}} \right) \tag{4}$$

For the Langmuir waves (L waves), the time evolution equation includes the effects of spontaneous emission and induced emission [10],

$$\frac{\partial I_{\mathbf{k}}^{\sigma L}}{\partial t} = \frac{4\pi e^2}{m_e k^2} \int d\mathbf{v}\, \delta(\sigma\omega_{\mathbf{k}}^L - \mathbf{k}\cdot\mathbf{v}) \times \left(\hat{n} e^2 f_e(\mathbf{v}) + \pi(\sigma\omega_{\mathbf{k}}^L)\, \mathbf{k} \cdot \frac{\partial f_e(\mathbf{v})}{\partial \mathbf{v}}\, I_{\mathbf{k}}^{\sigma L} \right) \tag{5}$$

For the ion sound waves (S waves), the time evolution equation containing only the terms corresponding to induced and spontaneous effects is as follows [10],

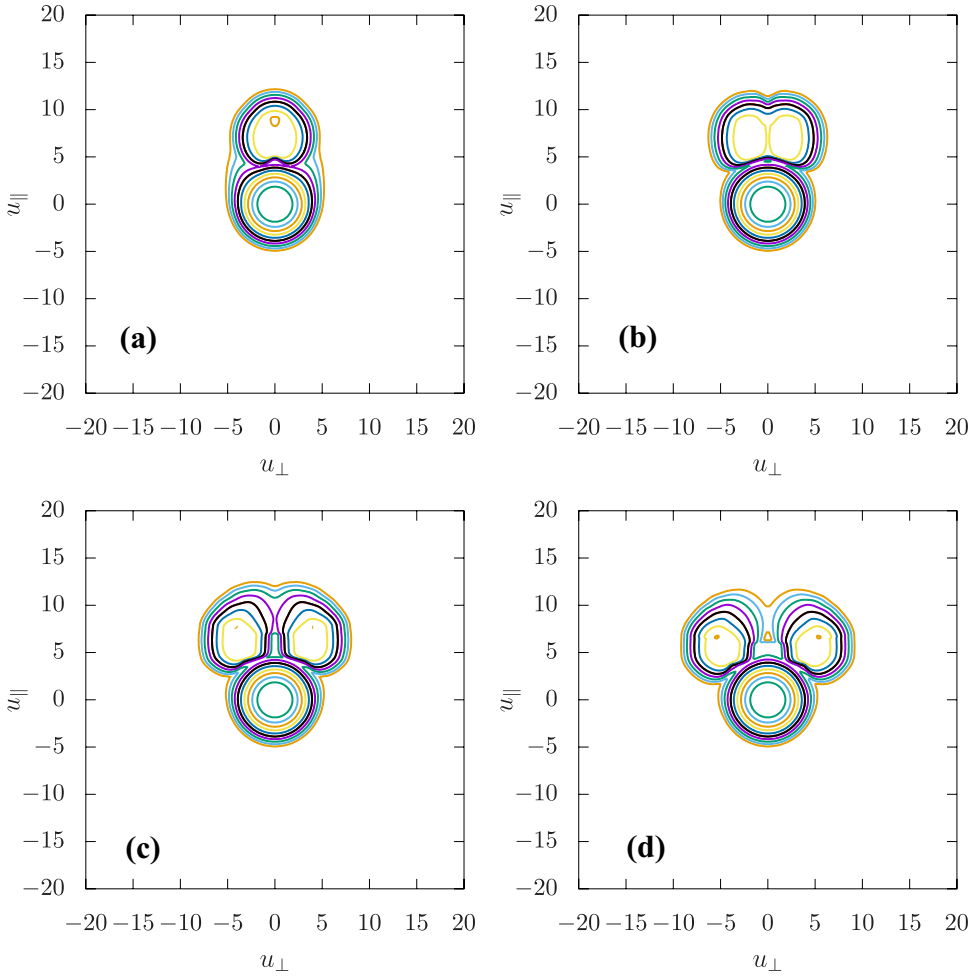

Fig. 3 Surface plots of the normalized electron distribution function in logarithmic scale, in bi-dimensional normalized velocity space, at $\tau = 500$. **a** $\theta_f = 0°$; **b** $\theta_f = 15°$; **c** $\theta_f = 30°$; **d** $\theta_f = 40°$. The level curves are as in Fig. 1. Other parameters and conditions are as in Fig. 1

$$\frac{\partial}{\partial t}\frac{I^{\sigma S}_{\mathbf{k}}}{\mu^S_{\mathbf{k}}} = \mu^S_{\mathbf{k}}\sigma\omega^L_{\mathbf{k}}\frac{4\pi e^2}{m_e k^2}\int d\mathbf{v}\;\delta(\sigma\omega^S_{\mathbf{k}} - \mathbf{k}\cdot\mathbf{v})$$
$$\times\left[\hat{n}\,e^2\,[f_e(\mathbf{v}) + f_i(\mathbf{v})] + \pi\,(\sigma\omega^L_{\mathbf{k}})\right. \tag{6}$$
$$\left.\times\left(\mathbf{k}\cdot\frac{\partial f_e(\mathbf{v})}{\partial\mathbf{v}} + \frac{m_e}{m_i}\,\mathbf{k}\cdot\frac{\partial f_i(\mathbf{v})}{\partial\mathbf{v}}\right)\frac{I^{\sigma S}_{\mathbf{k}}}{\mu^S_{\mathbf{k}}}\right],$$

where

$$\mu^S_{\mathbf{k}} = k^3\lambda^3_{De}\left(\frac{m_e}{m_i}\right)^{1/2}\left(1 + \frac{3T_i}{T_e}\right)^{1/2}.$$

$\lambda_{De} = v_e/(\sqrt{2}\omega_{pe})$ represents the Debie length, where $\omega_{pe} = \sqrt{4\pi n_e e^2/m_e}$ is the electron plasma angular frequency. m_i and T_i are the ion mass and the ion temperature in units of energy, respectively.

3 Numerical Results

For convenience of the numerical analysis, we define dimensionless quantities. A normalized velocity is defined by $\mathbf{u} = \mathbf{v}/v_e$, a normalized wave number by $\mathbf{q} = \mathbf{k}v_e/\omega_{pe}$, the normalized time variable by $\tau = \omega_{pe}t$, and the normalized wave frequency for waves of type α by $z^\alpha_{\mathbf{q}} = \omega^\alpha_{\mathbf{q}}/\omega_{pe}$ (where $\alpha = L$ or S). A normalized wave intensity for waves of type α is defined as follows,

$$\mathcal{E}^{\sigma\alpha}_{\mathbf{q}} = \frac{(2\pi)^2 g}{m_e v_e^2}\frac{I^{\sigma\alpha}_{\mathbf{k}}}{\mu^\alpha_{\mathbf{k}}}, \tag{7}$$

where $g = \left[2^{3/2}(4\pi)^2 n_e\lambda^3_{De}\right]^{-1}$, and it is defined that $\mu^L_{\mathbf{k}} = 1$. Other dimensionless quantities are the normalized speed, $u = v/v_e$, and the normalized thermal velocities $u_\beta = v_\beta/v_e$, where $v_\beta = \sqrt{2T_\beta/m_\beta}$ is the thermal velocity of particles

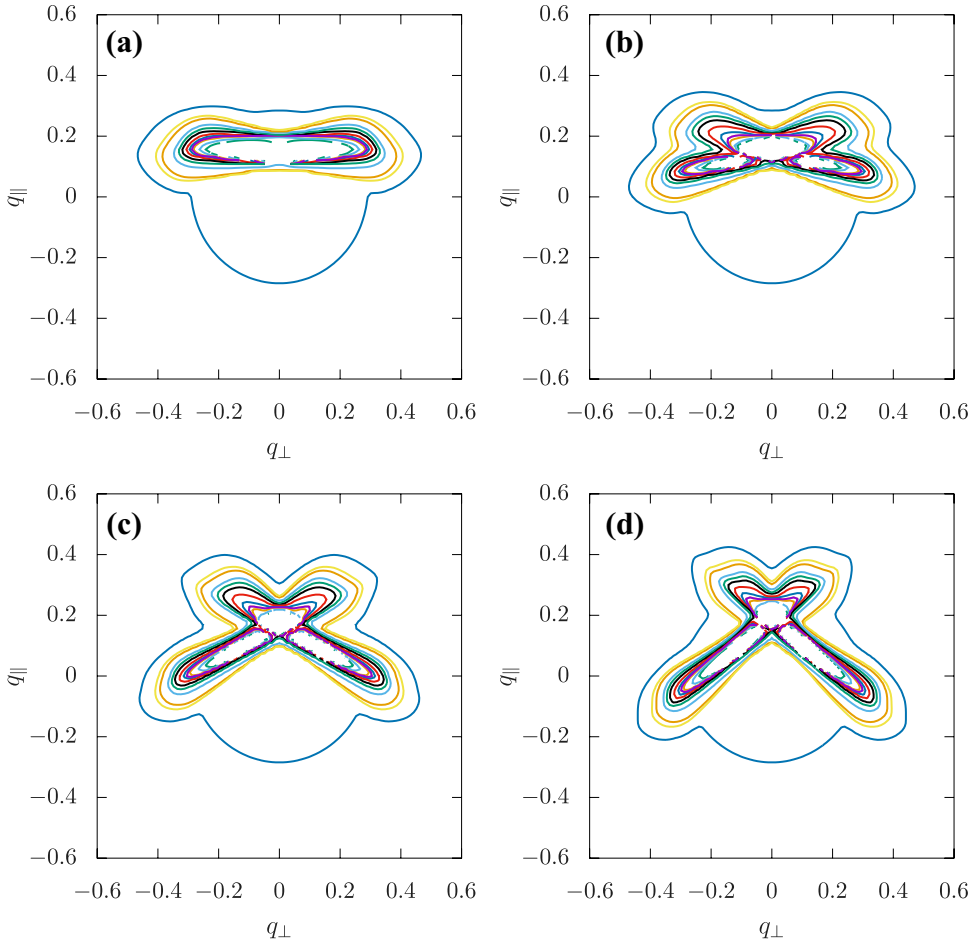

Fig. 4 Surface plots of the normalized spectrum of Langmuir waves in logarithmic scale, vs. $q_\parallel = k_\parallel v_e/\omega_{pe}$ and $q_\perp = k_\perp v_e/\omega_{pe}$, at $\tau = 500$. **a** $\theta_f = 0°$; **b** $\theta_f = 15°$; **c** $\theta_f = 30°$; **d** $\theta_f = 40°$. The level curves are as in Fig. 2. Other parameters and conditions are as in Fig. 1

of type β. An immediate consequence of these definitions is that $u_e = 1$.

The dispersion relations for L and S waves, written in terms of the nondimensional variables, are as follows,

$$z_{\mathbf{q}}^L = \left(1 + \frac{3}{2}q^2\right)^{1/2}, \tag{8}$$

$$z_{\mathbf{q}}^S = \frac{q}{\sqrt{2}}\left(\frac{m_e}{m_i}\right)^{1/2}\left(1 + 3\frac{T_i}{T_e}\right)^{1/2}\left(1 + \frac{1}{2}q^2\right)^{-1/2}. \tag{9}$$

For initialization of the wave spectra, Eqs. (5) and (6) are utilized, taking into account only the background Maxwellian core, and balancing the effects of the spontaneous and induced emission terms. The procedure leads to the following expressions for the initial wave spectra:

$$\mathcal{E}_{\mathbf{q}}^{\sigma L} = \frac{g}{2(z_{\mathbf{q}}^L)^2}, \quad \mathcal{E}_{\mathbf{q}}^{\sigma S} = \frac{g}{2(z_{\mathbf{q}}^L)(z_{\mathbf{q}}^S)}. \tag{10}$$

In addition to the use of dimensionless quantities for the set of kinetic Eqs. (4), (5), and (6), we also utilize a two-dimensional (2D) approximation, a useful approximation for the description of three-dimensional systems with azimuthal symmetry. Therefore, the normalized particle velocities are given by $\mathbf{u} = u_\perp \mathbf{e}_\perp + u_\parallel \mathbf{e}_\parallel$, and the normalized wave numbers are given by $\mathbf{q} = q_\perp \mathbf{e}_\perp + q_\parallel \mathbf{e}_\parallel$, where $\mathbf{e}_\parallel$ is along the direction of the ambient magnetic field. In the 2D approach, and using the normalized variables, the electron velocity distribution function becomes as follows:

$$\Phi_{e,M}(\mathbf{u}) = \frac{1}{\pi u_e^2}\exp\left(-\frac{(u_\perp^2 + (u_\parallel - u_0)^2}{u_e^2}\right), \tag{11}$$

$$\Phi_{e,f}(\mathbf{u}) = \frac{1}{\pi u_e^2}\exp\left(-\frac{(u_\perp - u_{f\perp})^2 + (u_\parallel - u_{f\parallel})^2}{u_e^2}\right), \tag{12}$$

Equations (4), (5), and (6) are then transformed into a set of finite difference equations, for numerical solution. We use a *splitting* method with fixed time step to solve Eq. (4), and a Runge-Kutta procedure with the same time step to solve Eqs. (5) and (6). As time step, we use , with a 51×51 grid point covering the region $0 \le q_\perp \le 0.6$ and $0 \le q_\parallel \le 0.6$ in wave number space, and a 169×337 grid point covering the region $0 \le u_\perp \le 20$ and

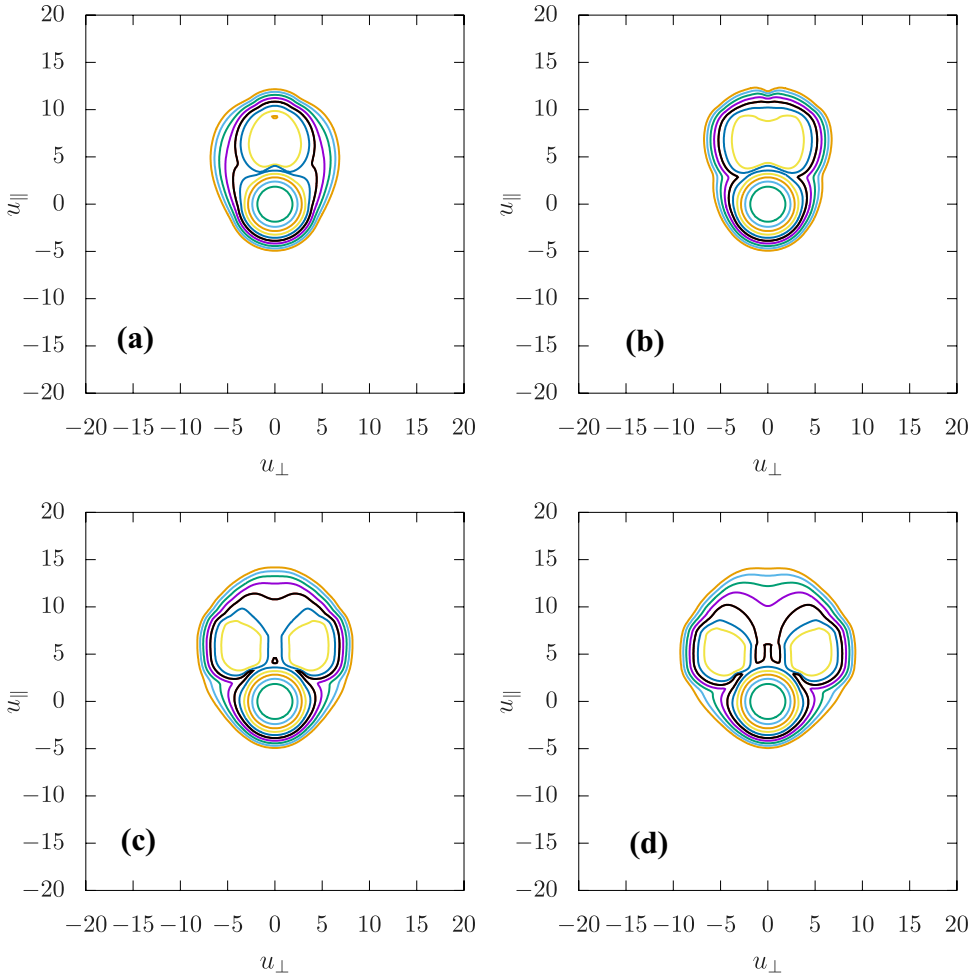

Fig. 5 Surface plots of the normalized electron distribution function in logarithmic scale, in bi-dimensional normalized velocity space, at $\tau = 1000$. **a** $\theta_f = 0°$; **b** $\theta_f = 15°$; **c** $\theta_f = 30°$; **d** $\theta_f = 40°$. The level curves are as in Fig. 1. Other parameters and conditions are as in Fig. 1

$-20 \leq u_\parallel \leq 20$. Similar values of grid size in wave number space had already been used in previous studies, as in refs. [11, 12], for instance. In velocity space, however, the present analysis utilizes a grid size larger than that utilized in these previous studies, in order to improve the conditions for visualization of extended electron tails, if they are produced along the dynamics of the system. As parameters for the numerical analysis, we utilize $\left(n_e \lambda_{De}^3\right)^{-1} = 5.0 \times 10^{-3}$, $n_{fe}/n_e = 1.0 \times 10^{-3}$, $u_f = 8.0$, $T_f/T_e = 1.0$, and $T_e/T_i = 2.0$.

In the sequence of Figs. 1, 2, 3, 4, 5, 6, 7, 8, 9, and 10, we show results of the numerical analysis in the form of surface plots of the normalized electron distribution function in logarithmic scale, vs. $u_\parallel$ and $u_\perp$, and surface plots of the normalized spectrum of Langmuir waves, in logarithmic scale, vs. $q_\parallel$ and $q_\perp$. These figures have been obtained considering several values of the beam pitch angle, and several moments along time evolution. Figures 1, 2, 3, 4, 5, 6, 7, 8, 9, and 10 display four panels, corresponding to results obtained with $\theta_f = 0°$ in panel a, $\theta_f = 15°$ in panel b, $\theta_f = 30°$ in panel c, and $\theta_f = 40°$ in panel d.

Figure 1 displays surface plots of the normalized electron distribution function, at $\tau = 100$. At this early stage in the time evolution, the distribution function is still very close to the initial shape. In Fig. 1a, the case of $\theta_f = 0°$ displays the presence of the beam propagating along the parallel direction, and the occurrence of the region of positive velocity derivatives between the core distribution and the beam. In panel b, it is seen the case of $\theta_f = 15°$. The ring-beam appears in the 2D plot in the form of two detached beams, with two mirrored regions of positive derivative in velocity space. Panels c and d of Fig. 1, depicting the cases of $\theta_f = 30°$ and $\theta_f = 40°$, respectively, show similar structures in velocity space, with regions of positive derivatives progressively detached in velocity space.

Figure 2 shows surface plots of the normalized spectrum of Langmuir waves in logarithmic scale, vs. $q_\parallel$ and $q_\perp$, also at $\tau = 100$. The parameters and conditions are the same as those used to obtain Fig. 1. Figure 2a, which shows the case of $\theta_f = 0°$, exhibits the peak of forward propagating L waves which is generated by the beam aligned with the parallel direction. In Fig. 2b, which shows the case of $\theta_f = 15°$, it

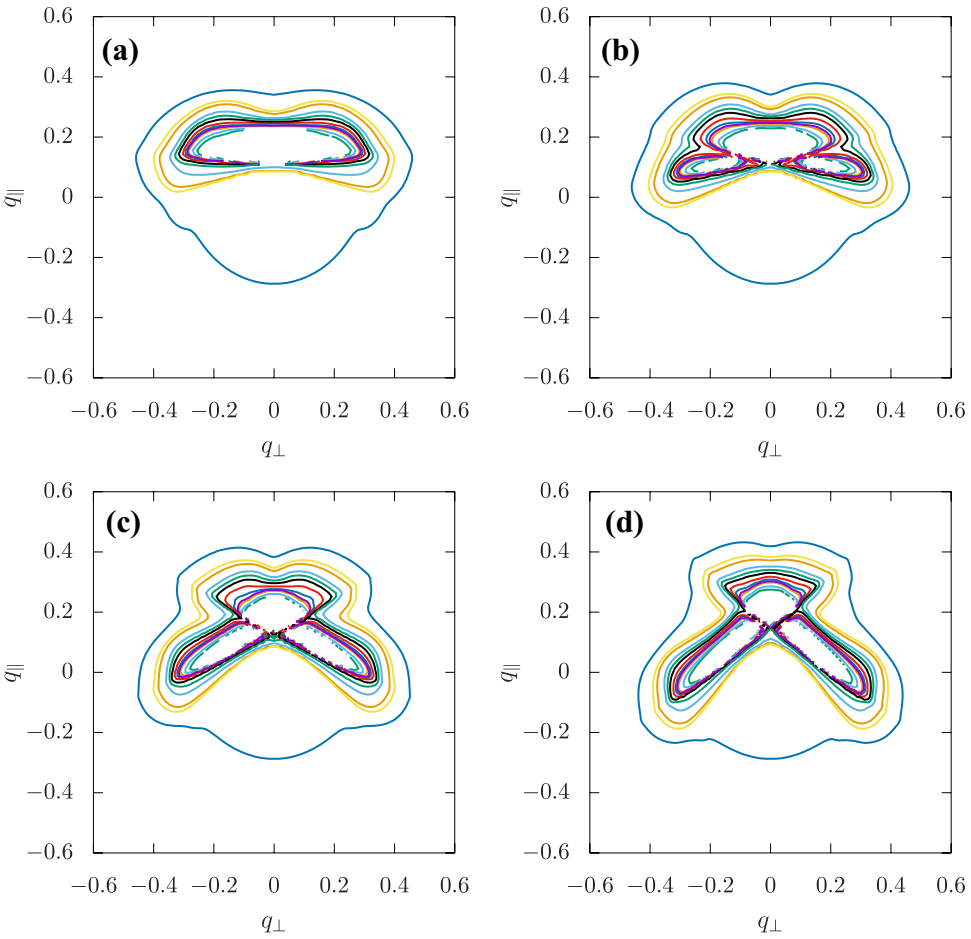

Fig. 6 Surface plots of the normalized spectrum of Langmuir waves in logarithmic scale, vs. $q_\parallel = k_\parallel v_e/\omega_{pe}$ and $q_\perp = k_\perp v_e/\omega_{pe}$, at $\tau = 1000$. **a** $\theta_f = 0°$; **b** $\theta_f = 15°$; **c** $\theta_f = 30°$; **d** $\theta_f = 40°$. The level curves are as in Fig. 2. Other parameters and conditions are as in Fig. 1

is seen that the two separated regions of positive derivative which appear in the surface plots of the distribution function, in Fig. 1b, generate two peaks of L waves, which cross each other forming a structure similar to the letter X. The maximum of this structure is a peak of forward propagating waves, around $q_\perp = 0$ where the two generated peaks add constructively. Figure 2c, d show the cases of $\theta_f = 30°$ and $\theta_f = 40°$, respectively. The X structure is present in both cases, progressively more pronounced. It can be noticed that in the cases of panels c and d significant amplitude of L waves is seen at $q_\parallel \simeq 0$, with finite $q_\perp$, while in panels a and b the significant amplitudes occur only for positive values of $q_\parallel$.

In Fig. 3, it is depicted a set of panels with surface plots of the normalized electron distribution function in logarithmic scale, at $\tau = 500$. By comparison with the corresponding panels is Fig. 1, it is seen that at $\tau = 500$ the top of the beam distribution is already well flattened, forming a *plateau* in velocity space, but a region of positive velocity derivatives still exists between the core and the beam distribution. Figure 3c, d show an increase in the electron population with $u_\parallel \simeq 10$ and $u_\perp \simeq 0$, in comparison with Fig. 1c, d.

Figure 4 shows the surface plots of the normalized spectrum of Langmuir waves in logarithmic scale, at $\tau = 500$, corresponding to the distribution functions depicted in Fig. 3. By comparison with Fig. 2, it is seen that the structure of L waves in wave number space keeps the same form, but the peaks which are formed have become higher and somewhat wider.

At $\tau = 1000$, Fig. 5a, b show that in the case of zero or moderate pitch angle a single *plateau* is formed in the velocity distribution function, indicating that the ring-beam has become a single wide beam. In Fig. 5c, d, it is seen that significant increase in the high parallel velocity has occurred, indicating significant electron acceleration by the quasilinear interaction with the ring-beam population. The corresponding surface plots of the normalized spectra of L waves appear in Fig. 6. By comparison with Fig. 4, it is seen that the peaks in the L spectra continue to grow in amplitude, and become appreciably wider. Particularly, by comparing panels c and d of Figs. 4 and 6, it is seen that the amplitude of L waves at $q_\parallel \simeq 0$ and finite $q_\perp$, in the cases of $\theta_f = 30°$ and $\theta_f = 40°$ is considerably higher at $\tau = 1000$ than at $\tau = 500$.

Figures 7 and 8 display the surface plots of the normalized electron distribution function in logarithmic scale and the surface plots of the normalized spectrum of Langmuir waves in logarithmic scale, respectively, at $\tau = 2000$. The

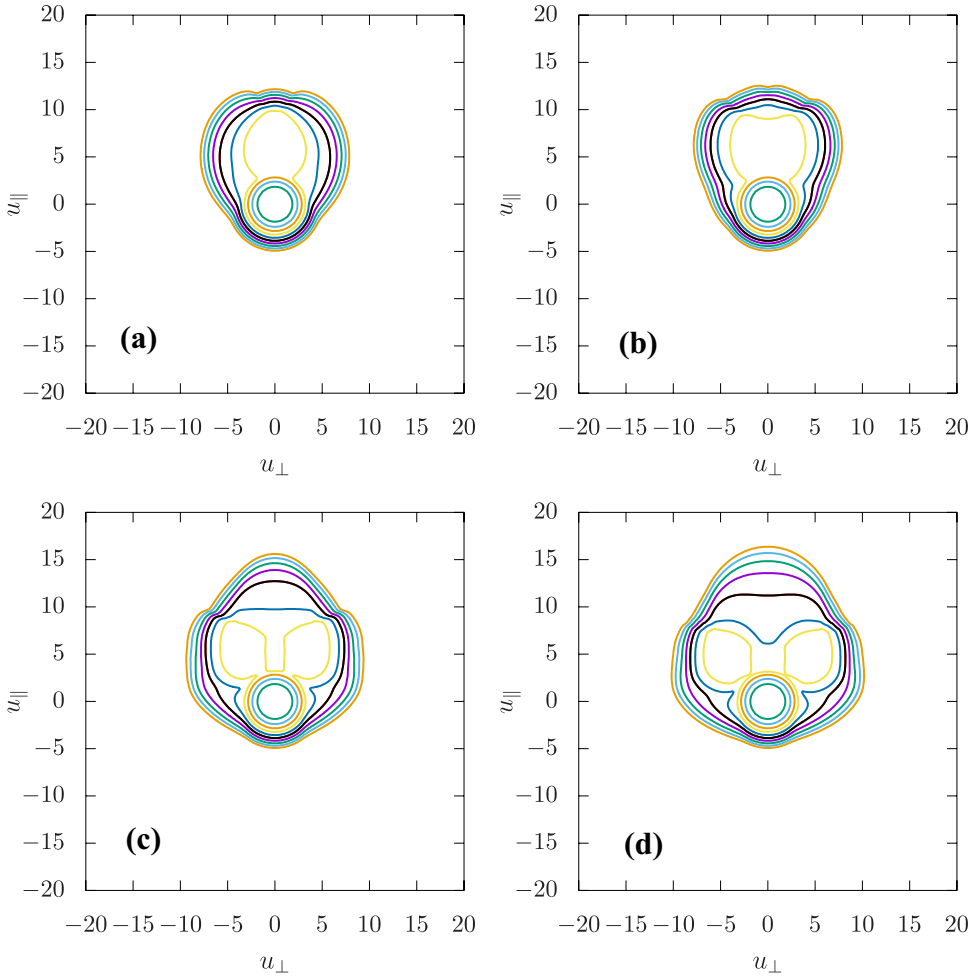

Fig. 7 Surface plots of the normalized electron distribution function in logarithmic scale, in bi-dimensional normalized velocity space, at $\tau = 2000$. **a** $\theta_f = 0°$; **b** $\theta_f = 15°$; **c** $\theta_f = 30°$; **d** $\theta_f = 40°$. The level curves are as in Fig. 1. Other parameters and conditions are as in Fig. 1

patterns seen in Figs. 5 and 6 continue to be seen in Figs. 7 and 8, only more pronounced. The presence of accelerated electrons along the parallel direction is very conspicuous, in the cases of significant pitch angle, as $\theta_f = 30°$ in Fig. 7c and $\theta_f = 40°$ in Fig. 7d. Similar comments can be made about Figs. 9 and 10, which show respectively the electron distribution function and the L wave spectrum at $\tau = 3000$.

The evolution of the high-velocity tail in the electron velocity distribution can be appreciated from another perspective in Fig. 11, which shows the velocity distribution as a function of $u_\parallel$, after integration along $u_\perp$, for several values of normalized time, $\tau = 100$, 200, 500, 1000, 2000, and 3000. The four panels of Fig. 11 display the cases of $\theta_f = 0°$, in panel a, $\theta_f = 15°$ in panel b, $\theta_f = 30°$ in panel c, and $\theta_f = 40°$ in panel d. The high-velocity tail is barely perceptible in the case of small pitch angle of the beam distribution, as in Fig. 11a, b, and clearly defined for the cases of $\theta_f = 30°$ and $\theta_f = 40°$, seen in Fig. 11c, d. Although the formation of high-velocity electron tails has already been reported [13], associated to nonlinear effects, the acceleration of electrons by quasilinear effects, in association with ring-beam electron distributions, has not yet been reported in the literature, as far as we are aware.

The mechanism for generation of the high-velocity distribution by quasilinear effects, in the case of ring-beam distributions with significant pitch angle, is as follows. In two dimensions, and in terms of nondimensional variables, the resonance condition for wave particle interaction involving L waves is given by

$$\sigma z_q^L - q_\perp u_\perp - q_\parallel u_\parallel = 0$$

Considering for instance the case of $\theta_f = 30°$, Fig. 7c shows that at $\tau = 2000$ the velocity derivative is very significant for $u_\parallel \simeq 2.0$ and $u_\perp \simeq 3.5$. Considering $\omega_q^L \simeq \omega_{pe}$ and $\sigma = 1$, and $q_\perp = 0.24$, the resonance condition is satisfied by

$$q_\parallel \simeq \frac{1 - q_\perp u_\perp}{u_\parallel} \simeq 0.08$$

The resonance condition appears in Eq. (5), for the evolution of L waves, and therefore shows that significant wave

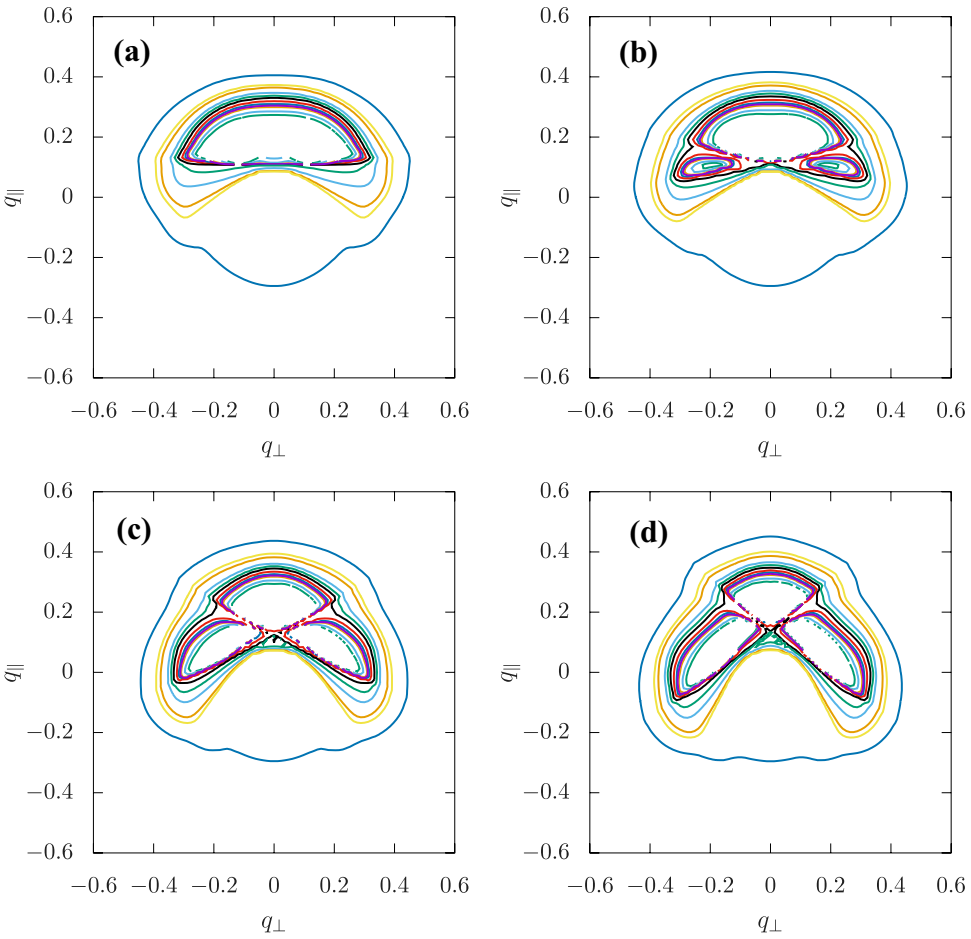

Fig. 8 Surface plots of the normalized spectrum of Langmuir waves in logarithmic scale, vs. $q_\parallel = k_\parallel v_e/\omega_{pe}$ and $q_\perp = k_\perp v_e/\omega_{pe}$, at $\tau = 2000$. **a** $\theta_f = 0°$; **b** $\theta_f = 15°$; **c** $\theta_f = 30°$; **d** $\theta_f = 40°$. The level curves are as in Fig. 2. Other parameters and conditions are as in Fig. 1

growth may occur for $q_\parallel \simeq 0.08$, $q_\perp \simeq 0.24$, which is near the extremity of one of the legs of the letter X, as seen in Fig. 8c. On the other hand, the same resonance condition appears in the equation for the evolution of the electron distribution function (Eq. 4). At the region $u_\perp \simeq 0$, the waves at the extremity of the letter X will be resonant with particles with the following parallel velocity,

$$u_\parallel \simeq \frac{1 - q_\perp u_\perp}{q_\parallel} \simeq 12,5$$

This result shows that waves at the tip of the X-type growth in the L wave spectrum, formed by quasilinear effect by resonance with the ring-beam distribution, can be resonant with particles with large parallel velocity, in a region of the distribution function where the velocity derivative is negative. The resonance process therefore leads to absorption of wave energy. That is, the ring-beam particles are able to transfer energy and accelerate particles in the region of high parallel velocity, by means of the spectrum of L waves generated by quasilinear growth.

The efficiency of the acceleration by the quasilinear process depends on the value of the pitch angle. The results which we have obtained indicate that for very large values of the pitch angle the efficiency is smaller than in the case of an intermediate pitch angle. For instance, Fig. 12a shows surface plots of the spectrum of L waves obtained for the case of $\theta_f = 60°$, at $\tau = 3000$. The comparison with the case of $\theta_f = 40°$ at the same time, seen in Fig. 10d, shows that in the case of a very large pitch angle the primary peak of L waves, around $q_\parallel = 0.3$, is much less pronounced than in the case of the intermediate pitch angle.

It is also seen that the tip of the X-type growth in the L spectrum goes well beyond $q_\parallel = 0$, toward the region of negative values of parallel wave number. The corresponding surface plots of the electron distribution appear at Fig. 12b, and show that in comparison with the case of $\theta_f = 40°$ seen in Fig. 9d the distribution function in the case of $\theta_f = 60°$ is broadened along the $u_\perp$ direction, and less extended along the $u_\parallel$ direction. Another perspective is seen in Fig. 12c, which shows 1D plots of the electron distribution function, at $\tau = 3000$, for several values of θ_f. It is seen that in the case of $\theta_f = 15°$ (green line)

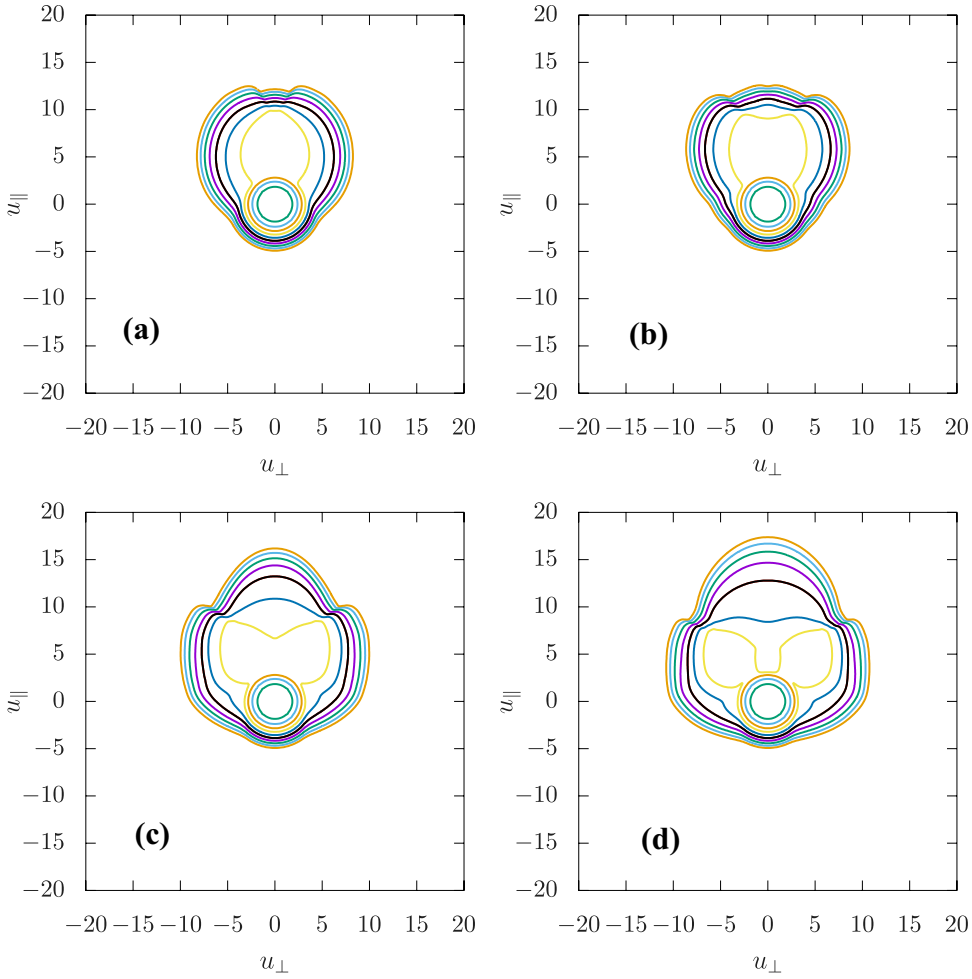

Fig. 9 Surface plots of the normalized electron distribution function in logarithmic scale, in bi-dimensional normalized velocity space, at $\tau = 3000$. **a** $\theta_f = 0°$; **b** $\theta_f = 15°$; **c** $\theta_f = 30°$; **d** $\theta_f = 40°$. The level curves are as in Fig. 1. Other parameters and conditions are as in Fig. 1

the distribution function is very similar to that obtained in the case without pitch angle, with $\theta_f = 0°$ (magenta line). The green line in almost indistinguishable of the magenta line, in the scale of the figure. There is a *plateau* in the region of the beam, without a significant electron tail beyond this *plateau*. For $\theta_f = 30°$ (blue line), the *plateau* is shorter than in the case of $\theta_f = 15°$, but an extended electron tail is seen in the region of high parallel velocity. For $\theta_f = 40°$ (red line), the extended electron tail is more pronounced, with the tail population overtaking the population obtained for $\theta_f = 30°$ around $u_\parallel \simeq 13$, where $\Phi_e \simeq 1 \times 10^{-7}$. On the other hand, for a large pitch angle, illustrated by the case of $\theta_f = 60°$ (black line), the *plateau* in the distribution is very short, and the extended electron tail which is formed does not overtake the tail formed in the case of $\theta_f = 40°$, even down below the level of $\Phi_e \simeq 1 \times 10^{-12}$.

We now investigate what is the effect of taking into account nonlinear effects in the equations for the wave amplitudes, on the acceleration of electrons which was demonstrated to occur in the case of ring-beam electron populations with sufficiently large beam pitch angle. For this investigation, we add at the right-hand side of Eq. (5) the following terms [10]

$$
\begin{aligned}
&+ \pi\sigma\omega^L_{\mathbf{k}}\,\frac{e^2}{2T_e^2}\sum_{\sigma',\sigma''=\pm1}\int d\mathbf{k}'\,\frac{\mu^S_{\mathbf{k}-\mathbf{k}'}\,(\mathbf{k}\cdot\mathbf{k}')^2}{k^2\,k'^2\,|\mathbf{k}-\mathbf{k}'|^2}\\
&\times\left(\sigma\omega^L_{\mathbf{k}}\,I^{\sigma' L}_{\mathbf{k}'}\,\frac{I^{\sigma'' S}_{\mathbf{k}-\mathbf{k}'}}{\mu^S_{\mathbf{k}-\mathbf{k}'}} - \sigma'\omega^L_{\mathbf{k}'}\,\frac{I^{\sigma'' S}_{\mathbf{k}-\mathbf{k}'}}{\mu^S_{\mathbf{k}-\mathbf{k}'}}\,I^{\sigma L}_{\mathbf{k}}\right.\\
&\left.-\sigma''\omega^L_{\mathbf{k}-\mathbf{k}'}\,I^{\sigma' L}_{\mathbf{k}'}\,I^{\sigma L}_{\mathbf{k}}\right)\delta(\sigma\omega^L_{\mathbf{k}} - \sigma'\omega^L_{\mathbf{k}'} - \sigma''\omega^S_{\mathbf{k}-\mathbf{k}'})
\end{aligned}
\tag{13}
$$

$$
\begin{aligned}
&- \sigma\omega^L_{\mathbf{k}}\,\frac{e^2}{\hat{n}\,m_e^2\,\omega_{pe}^2}\sum_{\sigma'}\int d\mathbf{k}'\int d\mathbf{v}\,\frac{(\mathbf{k}\cdot\mathbf{k}')^2}{k^2\,k'^2}\\
&\times\ \delta[\sigma\omega^L_{\mathbf{k}} - \sigma'\omega^L_{\mathbf{k}'} - (\mathbf{k}-\mathbf{k}')\cdot\mathbf{v}]\\
&\times\left[\frac{\hat{n}\,e^2}{\omega_{pe}^2}\left(\sigma'\omega^L_{\mathbf{k}'}\,I^{\sigma L}_{\mathbf{k}} - \sigma\omega^L_{\mathbf{k}}\,I^{\sigma' L}_{\mathbf{k}'}\right)[f_e(\mathbf{v}) + f_i(\mathbf{v})]\right.\\
&\left.-\ \pi\,\frac{m_e}{m_i}\,I^{\sigma' L}_{\mathbf{k}'}\,I^{\sigma L}_{\mathbf{k}}\,(\mathbf{k}-\mathbf{k}')\cdot\frac{\partial f_i(\mathbf{v})}{\partial\mathbf{v}}\right]
\end{aligned}
$$

where

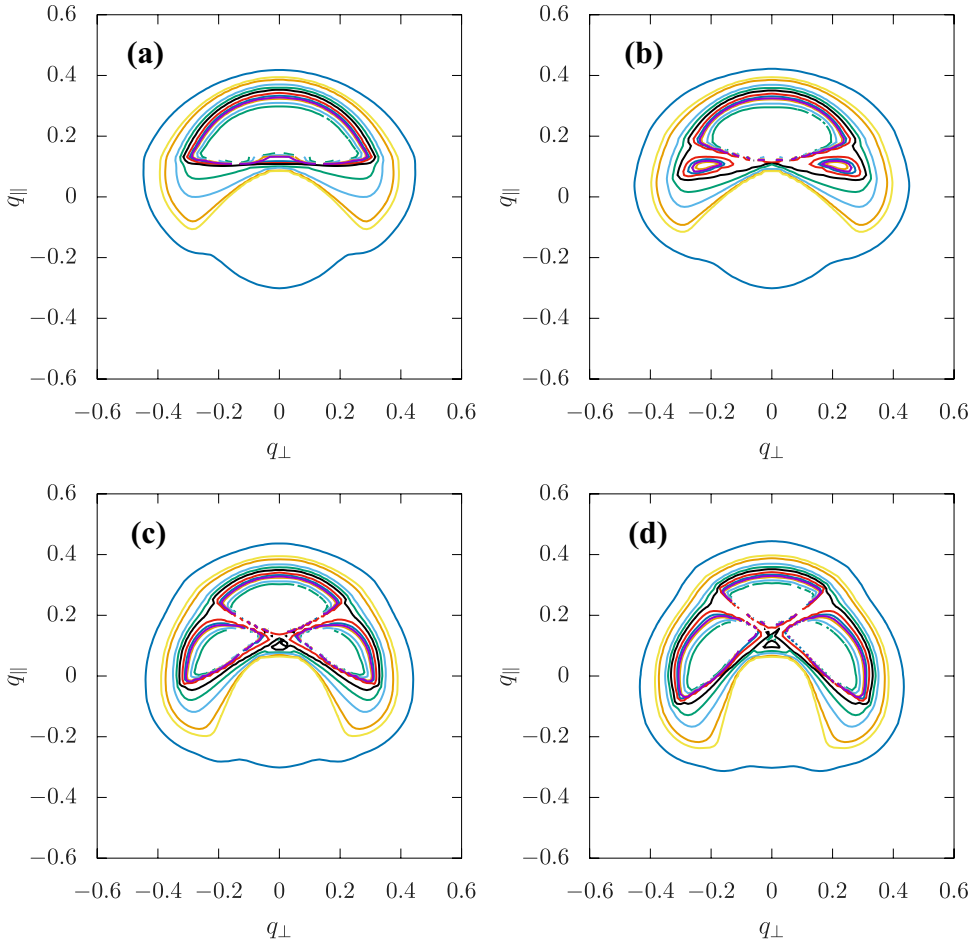

Fig. 10 Surface plots of the normalized spectrum of Langmuir waves in logarithmic scale, vs. $q_\parallel = k_\parallel v_e/\omega_{pe}$ and $q_\perp = k_\perp v_e/\omega_{pe}$, at $\tau = 3000$. **a** $\theta_f = 0°$; **b** $\theta_f = 15°$; **c** $\theta_f = 30°$; **d** $\theta_f = 40°$. The level curves are as in Fig. 2. Other parameters and conditions are as in Fig. 1

$$\mu_{\mathbf{k}}^S = |k|^3 \lambda_{De}^3 \left(\frac{m_e}{m_i}\right)^{1/2} \left(1 + \frac{3T_i}{T_e}\right)^{1/2} . \tag{14}$$

The first of these terms features the resonance condition $\delta(\sigma\omega_{\mathbf{k}}^L - \sigma'\omega_{\mathbf{k}'}^L - \sigma''\omega_{\mathbf{k}-\mathbf{k}'}^S)$, and describes the three-wave decay involving two L waves and one S wave. The second of these terms contains the resonance conditions $\delta[\sigma\omega_{\mathbf{k}}^L - \sigma'\omega_{\mathbf{k}'}^L - (\mathbf{k}-\mathbf{k}')\cdot\mathbf{v}]$, and represents the induced scattering term, involving two L waves.

At the right-hand side of Eq. (6), we add the term representing the three-wave decay, involving one S wave and two L waves, with resonance condition $\delta(\sigma\omega_{\mathbf{k}}^S - \sigma'\omega_{\mathbf{k}'}^L - \sigma''\omega_{\mathbf{k}-\mathbf{k}'}^S)$ [10],

$$+ \pi\sigma\omega_{\mathbf{k}}^L \frac{e^2}{4T_e^2} \sum_{\sigma',\sigma''} \int d\mathbf{k}' \frac{\mu_{\mathbf{k}}^S [\mathbf{k}'\cdot(\mathbf{k}-\mathbf{k}')]^2}{k^2 k'^2 |\mathbf{k}-\mathbf{k}'|^2}$$
$$\times \left(\sigma\omega_{\mathbf{k}}^L I_{\mathbf{k}'}^{\sigma' L} I_{\mathbf{k}-\mathbf{k}'}^{\sigma'' L} - \sigma'\omega_{\mathbf{k}'}^L I_{\mathbf{k}-\mathbf{k}'}^{\sigma'' L} \frac{I_{\mathbf{k}}^{\sigma S}}{\mu_{\mathbf{k}}^S} \right. \tag{15}$$
$$\left. -\sigma''\omega_{\mathbf{k}-\mathbf{k}'}^L I_{\mathbf{k}'}^{\sigma' L} \frac{I_{\mathbf{k}}^{\sigma S}}{\mu_{\mathbf{k}}^S} \right) \delta(\sigma\omega_{\mathbf{k}}^S - \sigma'\omega_{\mathbf{k}'}^L - \sigma''\omega_{\mathbf{k}-\mathbf{k}'}^L)$$

In order to illustrate the effects of the nonlinear processes in the time evolution of the spectrum of L waves, in the presence of a thermal core plus a ring-beam electron distribution, we present in Fig. 13 the surface plots of the normalized spectrum of Langmuir waves in logarithmic scale, vs. $q_\parallel$ and $q_\perp$, for the case of $\theta_f = 30°$, and for different moments along time evolution. Figure 13a–d represent the surface plots at $\tau = 100$, $\tau = 500$, $\tau = 1000$, and $\tau = 2000$, respectively. Figure 13a shows that the spectrum of L waves at $\tau = 100$ is very similar to that obtained for the same beam pitch angle and time, without taking into account nonlinear effects, shown in Fig. 2c. In Fig. 13b, the result obtained at $\tau = 500$ shows that, in addition to the X-like structure of L waves generated by quasilinear effect due to the ring-beam distribution, there is also the presence of the backward propagating L waves and of the ring-like structure in wave number space, which are structures generated by the processes of three-wave decay and scattering. Further along time evolution, Fig. 13c, d show that the wave structures which are due to nonlinear processes become more prominent, but the X-like structures due to quasilinear processes continue to be

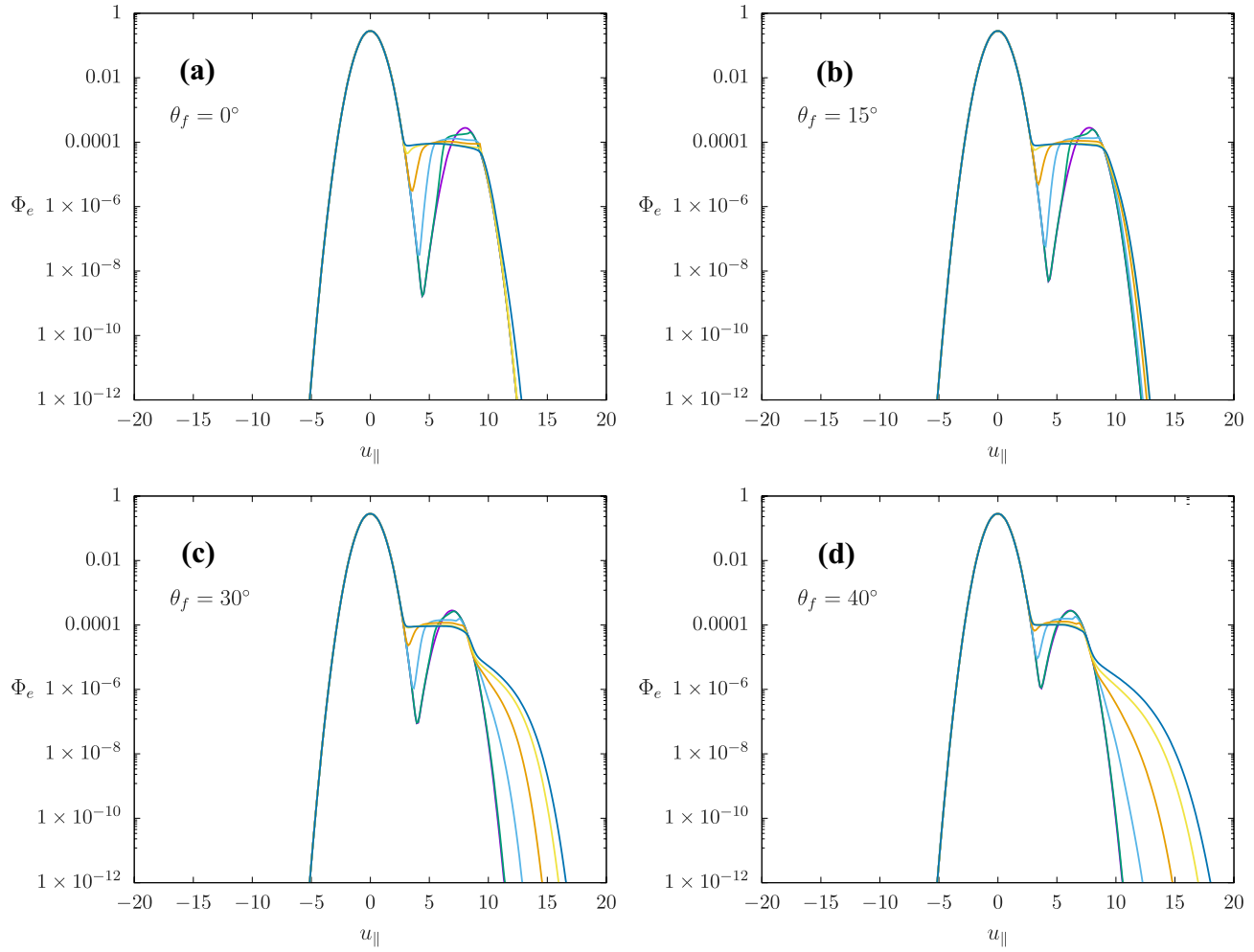

Fig. 11 Velocity distribution of electrons as a function of $u_\parallel$, after integration along $u_\perp$, at $\tau = 100$, 200, 500, 1000, 2000, and 3000. **a** $\theta_f = 0°$; **b** $\theta_f = 15°$; **c** $\theta_f = 30°$; **d** $\theta_f = 40°$. Other parameters and conditions are as in Fig. 1

very similar to those appearing in the corresponding figures obtained without taking into account nonlinear effect, which are Figs. 6c and 8d, respectively.

Figure 14 displays surface plots of the normalized electron distribution function in logarithmic scale, in two-dimensional normalized velocity space, for $\theta_f = 30°$, at the same time as the corresponding spectra of L waves appearing in Fig. 13. Figure 14a shows the distribution function at $\tau = 100$, practically identical to the distribution appearing in Fig. 1c. In Fig. 14b, it is depicted the case of $\tau = 500$, with a distribution very similar to the distribution appearing in Fig. 3c. At Fig. 14c, the case of $\tau = 1000$ shows surface plots which indicate a distribution function very similar to that appearing in Fig. 5c, only slightly widened in the region of the *plateau*. The widening of the distribution accelerates, so that in Fig. 14d the surface plots show a distribution with a *plateau* region noticeably larger than in the corresponding case without nonlinear effects (Fig. 7c).

Further evolution of the electron distribution function and of the L wave spectrum obtained taking into account nonlinear effects in the wave equations appears in Fig. 15, which shows results obtained at $\tau = 3000$. It is particularly noticeable that Fig. 15a shows the surface plots of the electron distribution function with a *plateau* considerably more extended than in the case of Fig. 9c, which was obtained without nonlinear effects, and also displaying a significant backward tail, formed due to absorption of energy of backward propagating waves.

Finally, we show in Fig. 16a one-dimensional plots of the velocity distribution of electrons obtained by taking into account nonlinear effects in the equations for the time evolution of the wave spectra, considering the case of $\theta_f = 30°$, as example of case with a ring-beam with significant pitch angle. Figure 16a shows the distribution function vs. $u_\parallel$, after integration along $u_\perp$, at $\tau = 100$, 200, 500, 1000, 2000, and 3000. Figure 16b also shows 1D plots of the electron distribution obtained for the case of $\theta_f = 30°$, but obtained

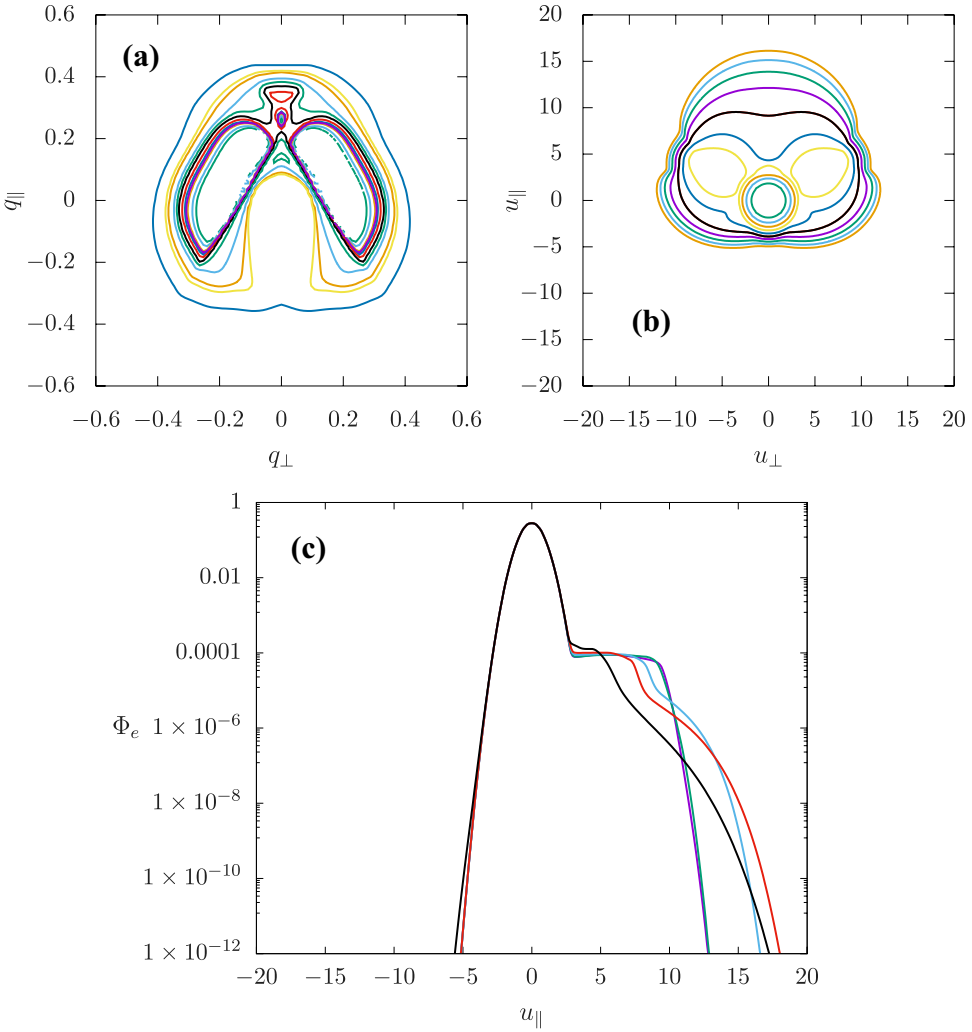

Fig. 12 **a** Surface plots of the normalized spectrum of Langmuir waves in logarithmic scale, vs. $q_\parallel = k_\parallel v_e/\omega_{pe}$ and $q_\perp = k_\perp v_e/\omega_{pe}$, at $\tau = 3000$, for $\theta_f = 60°$. The level curves are as in Fig. 2. **b** Surface plots of the normalized electron distribution function in logarithmic scale, in bi-dimensional normalized velocity space, at $\tau = 3000$, for $\theta_f = 60°$. **c** Velocity distribution of electrons as a function of $u_\parallel$, after integration along $u_\perp$, at $\tau = 3000$, for $\theta_f = 0°$ (magenta line), $\theta_f = 15°$ (green line), $\theta_f = 30°$ (blue line), $\theta_f = 40°$ (red line), and $\theta_f = 60°$ (black line). The level curves are as in Fig. 1. Other parameters and conditions are as in Fig. 1

without taking into account nonlinear effects. It is the same as Fig. 11c, and it is reproduced here to facilitate the comparison between the two cases. The comparison between these figures shows that the maximum velocity charactering the end of the high-velocity electron tail is similar in the two cases, but it is seen that the density of the high-velocity population is enhanced when the nonlinear effects are taken into account, in comparisons with the results obtained without taking into account these effects.

4 Final Remarks

We have presented results obtained from numerical analysis of a set of equations of weak turbulence theory, considering initial conditions in which a tenuous ring-beam electron distribution is moving through a background Maxwellian plasma. The study can be considered complementary to the analysis presented in ref. [9], but in the present paper we have emphasized conditions leading to the formation of extended electron tails, which have been shown to be connected with the occurrence of significant pitch angle in the velocity of the electron beam.

The first results presented in the paper have been obtained by taking into account only the mechanisms of spontaneous and induced emission in the equation for the amplitudes of electrostatic waves, with the neglect of nonlinear effects. These results have shown that, in the case of sufficiently significant pitch angle, there is substantial growth of amplitude for waves at the region of very small values of $k_\parallel$ and finite values of $k_\perp$, and these waves are resonant with electrons at large values of parallel velocity, beyond the parallel beam velocity. These waves therefore lose energy to the resonant electrons at the far tail of the distribution. As a consequence, there is substantial growth of the high-velocity electron population, resulting an extended forward tail in the electron population. This electron acceleration due to quasilinear effects in the case of ring-beam distributions is an acceleration mechanism which has not yet been reported in the literature.

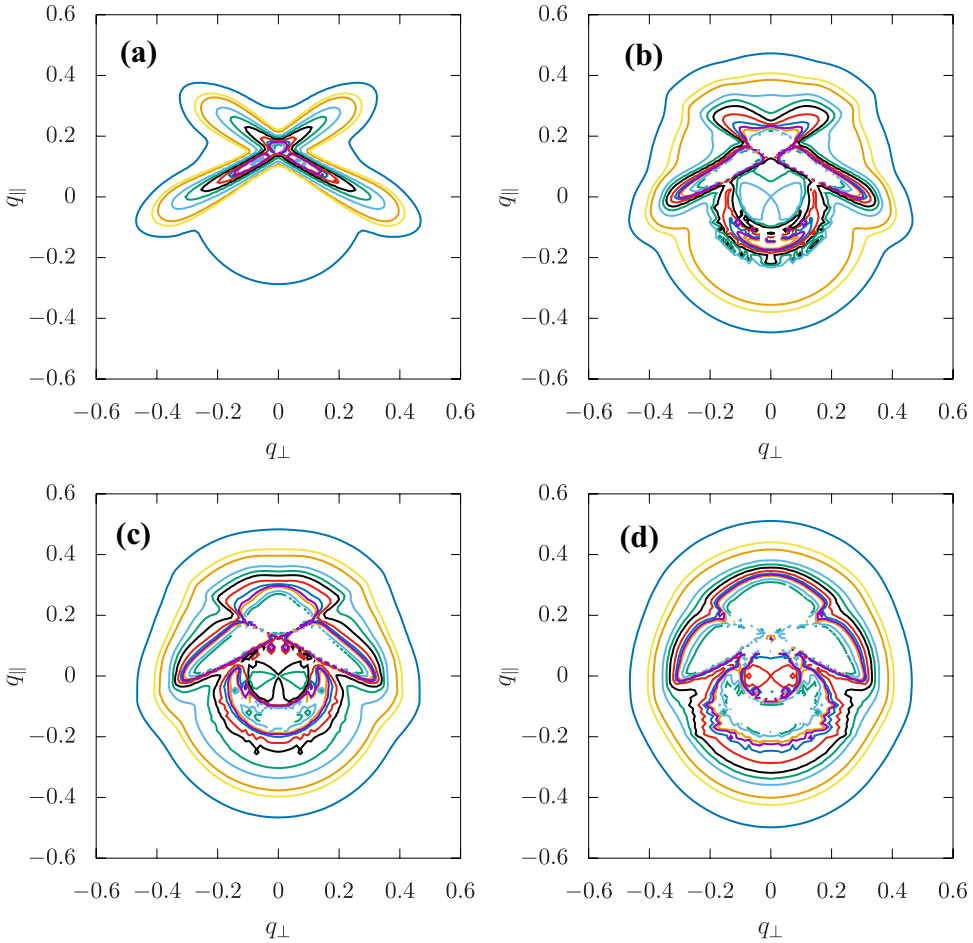

Fig. 13 Surface plots of the normalized spectrum of Langmuir waves in logarithmic scale, vs. $q_\parallel = k_\parallel v_e/\omega_{pe}$ and $q_\perp = k_\perp v_e/\omega_{pe}$, for $\theta_f = 30°$ and different moments along time evolution. **a** $\tau = 100$; **b** $\tau = 500$; **c** $\tau = 1000$; **d** $\tau = 2000$. Results obtained taking into account spontaneous and induced emission, three wave decay, and induced scattering, in the equation for evolution of Langmuir waves. The level curves are as in Fig. 2. Other parameters and conditions are as in Fig. 1

In the sequence, we have investigated the effect of nonlinear mechanisms on the evolution of this acceleration process, by taking into account the nonlinear mechanisms of three-wave decay in the equations for L and S waves, and also the mechanism of induced scattering in the equation for L waves. The presence of these nonlinear mechanisms leads to the appearing of a peak for L waves propagating in the backward direction, as well to the formation of a ring-like structure in wave number space for L waves, as already reported in studies which considered electron beams aligned with the parallel direction. The forward tail in the electron distribution function, for sufficiently large pitch angle of the beam velocity, is enhanced in the presence of nonlinear effects, in comparison with the situation where the nonlinear effects are neglected.

It may be added that numerical analysis had already shown that the Langmuir turbulence associated to the beam-plasma instability could generate energetic electron tails, as in ref. [13], in the case of distributions with asymmetric beams, along forward and backward directions. More recently, the asymptotic Langmuir turbulence has been shown to be a mechanism for generating a kappa tail in the electron distribution, in the context of a rigorous theory culminating with a steady-state solution of the system of coupled equations for the electron distribution and the Langmuir waves [14]. The novel aspect of the present paper is that it only takes the quasilinear process to produce the energetic tail. As it has been seen, the addition of nonlinear processes enhances the process, but even without such nonlinear effects in the case of ring-beam distributions the tail can be formed rapidly.

Finally, it can be remembered that the present investigation only considered ring-beam distributions with azimuthal symmetry, which are symmetric along the direction of perpendicular velocity, in a two-dimensional approximation. Velocity distributions without azimuthal symmetry would add another level of complexity to the numerical analysis, and can be the object of future research efforts.

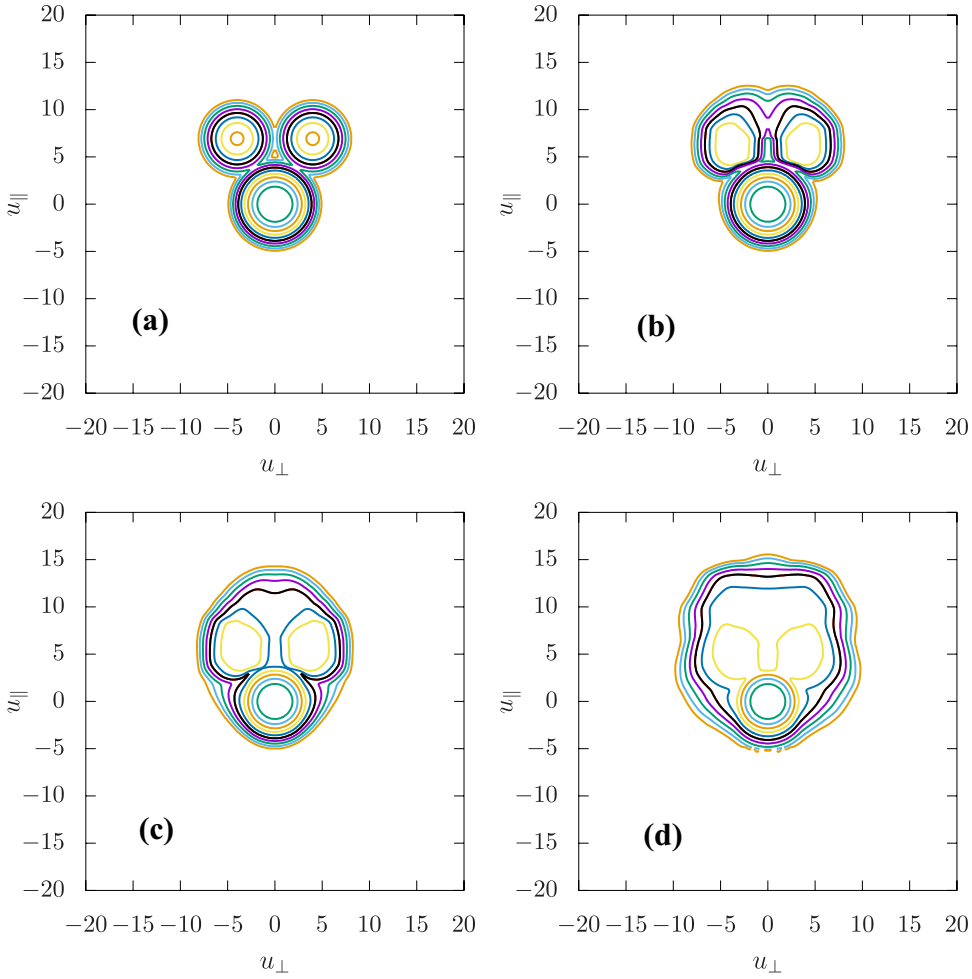

Fig. 14 Surface plots of the normalized electron distribution function in logarithmic scale, in bi-dimensional normalized velocity space, for $\theta_f = 30°$ and different moments along time evolution. **a** $\tau = 100$; **b** $\tau = 500$; **c** $\tau = 1000$; **d** $\tau = 2000$. The level curves are as in Fig. 1. Other parameters and conditions are as in Fig. 13

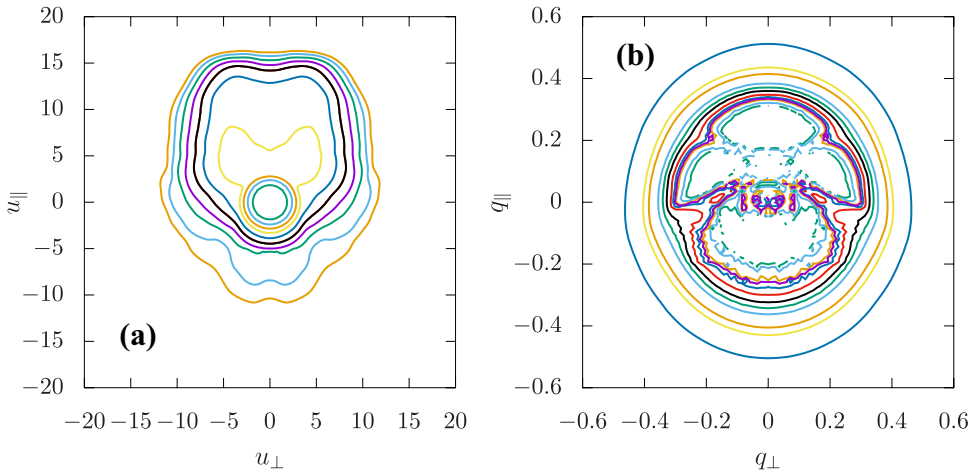

Fig. 15 **a** Surface plots of the normalized electron distribution function in logarithmic scale, in bi-dimensional normalized velocity space, for $\theta_f = 30°$ and $\tau = 3000$. The level curves are as in Fig. 1. **b** Surface plots of the normalized spectrum of transverse waves in logarithmic scale, vs. $q_\parallel = k_\parallel v_e/\omega_{pe}$ and $q_\perp = k_\perp v_e/\omega_{pe}$, for $\theta_f = 30°$ and $\tau = 3000$. The level curves are as in Fig. 2. Other parameters and conditions are as in Fig. 13

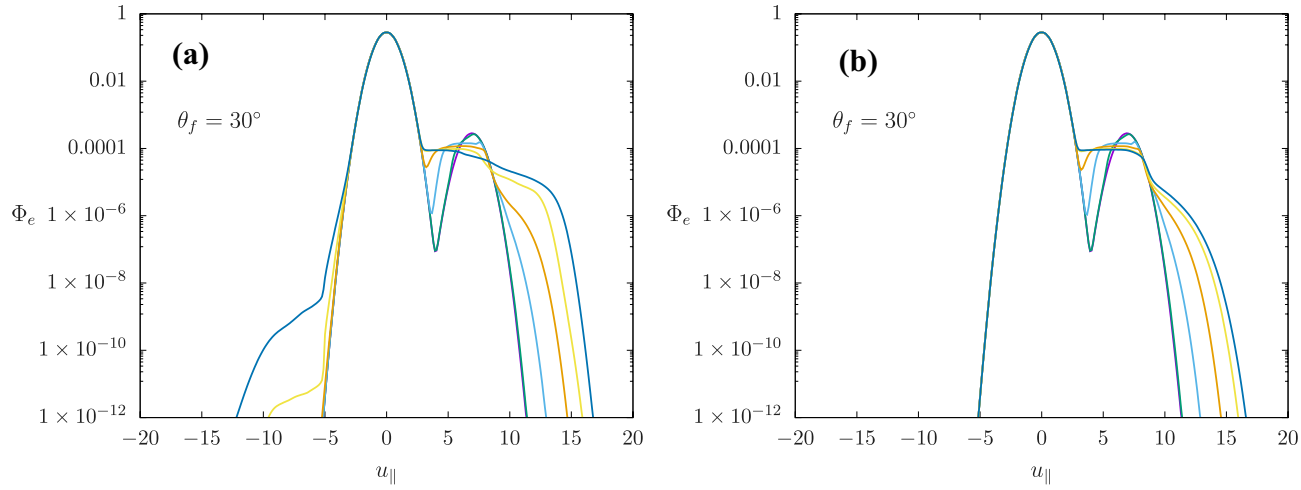

Fig. 16 **a** Velocity distribution of electrons as a function of $u_\parallel$, after integration along $u_\perp$, at $\tau = 100$, 200, 500, 1000, 2000, and 3000, for $\theta_f = 30°$. Other parameters and conditions are as in Fig. 13. **b** Velocity distribution of electrons as a function of $u_\parallel$, after integration along $u_\perp$, at $\tau = 100$, 200, 500, 1000, 2000, and 3000, for $\theta_f = 30°$ (same as Fig. 11c). Other parameters and conditions are as in Fig. 1

Funding LFZ acknowledges support from CNPq (Brazil), Grant No. 302708/2018-9, and partial support by the Coordenação de Aperfeiçoamento de Pessoal de Nível Superior - Brasil (CAPES) - Finance Code 001. PHY acknowledges NASA Grant No. NNH18ZDA001N-HSR and NSF Grants No. 1842643 and 2203321 to the University of Maryland.

Declarations

Ethics Approval This manuscript is original and has not been published elsewhere, and is not submitted to another journal. All authors have contributed to the work.

Competing Interests The authors declare no competing interests.

References

1. Z.-J. Tong, C.-B. Wang, P.-J. Zhang, J. Liu, Phys. Plasmas **24**, 052902 (2017). https://doi.org/10.1063/1.4982213
2. M. Horky, Y. Omura, O. Santolik, Phys. Plasmas **25**, 042905 (2018). https://doi.org/10.1063/1.5025912
3. M. Horky, Y. Omura, Phys. Plasmas **26**, 022904 (2019). https://doi.org/10.1063/1.5077094
4. X. Zhou, P.A. Munoz, J. Buechner, S. Liu, Astrophys. J. **891**, 92 (2020). https://doi.org/10.3847/1538-4357/ab6a0d
5. C.S. Wu, J. Geophys. Res. **89**, 8857 (1984). https://doi.org/10.1029/JA089iA10p08857
6. I.H. Cairns, S.A. Knock, P.A. Robinson, Z. Kuncic, in *Advances in Space Environment Research, chapter Type II solar radio bursts: Theory and space weather implications*, ed. by A.C.-L. Chian et al (Springer, Dordrecht, 2003)
7. I.H. Cairns, J. Geophys, Res. **93**, 858 (1988). https://doi.org/10.1029/JAo93iA02p00858
8. M. Karlický, M. Vandas, Planet. Space Sci. **55**, 2336 (2007). https://doi.org/10.1016/j.pss.2007.05.015
9. L.F. Ziebell, Astrophys. Space Sci. **366**, 60 (2021). https://doi.org/10.1007/s10509-021-03966-y
10. P.H. Yoon, L.F. Ziebell, R. Gaelzer, J. Pavan, Phys. Plasmas **19**, 102303, 9pp (2012). https://doi.org/10.1063/1.4757224
11. L.F. Ziebell, P.H. Yoon, R. Gaelzer, J. Pavan, Phys. Plasmas **21**, 012306 (2014). https://doi.org/10.1063/1.4863453
12. L.F. Ziebell, P.H. Yoon, L.T. Petruzzellis, R. Gaelzer, J. Pavan, Astrophys. J. **806**, 237 (2015). https://doi.org/10.1088/0004-637X/806/2/237
13. R. Gaelzer, L.F. Ziebell, A. Figueroa-Viñas, P.H. Yoon, C.-M. Ryu, Astrophys. J. **677**, 676 (2008). https://doi.org/10.1086/527430
14. P.H. Yoon, J. Geophys. Res. **119**, 7074 (2014). https://doi.org/10.1002/2014JA020353